Thermal Science and Engineering Progress 76 (2026) 104814

Contents lists available at ScienceDirect

Thermal Science and Engineering Progress

journal homepage: www.sciencedirect.com/journal/thermal-science-and-engineering-progress

Numerical analysis of the effect of 5G electromagnetic radiation on human head with metallic implants

Deepshikha Bhargava [a,*], Phadungsak Rattanadecho [b]

[a] Department of Mechanical Engineering, Faculty of Engineering, Kasetsart University, 50 Ngam Wong Wan Road, Ladyaow Chatuchak, Bangkok 10900, Thailand
[b] Center of Excellence in Electromagnetic Energy Utilization in Engineering (CEEE), Department of Mechanical Engineering, Faculty of Engineering, Thammasat University (Rangsit Campus), 99 Moo 18, Klong Luang, Pathum Thani 12120, Thailand

ARTICLE INFO

Keywords:
Medical implant
Human head
5G radiation
Mobile phone
SAR
Temperature
FEM

ABSTRACT

With the advent of 5G communication technologies, concerns regarding electromagnetic (EM) radiation exposure, particularly in individuals with metallic implants, have gained significant attention. This study investigates the interaction of 5G EM radiation with a two-dimensional (2D) heterogeneous human head model comprising six layers: skin, fat, bone, dura, cerebrospinal fluid (CSF), and brain. The model is exposed to 5G frequencies (2.6, 3.6, 4.4, and 6 GHz) at a power level of 1 W, both in the absence and presence of stainless steel 410 implants (pin- and sphere-shaped) embedded within the bone layer. A coupled model of EM wave propagation and bio-heat transfer is solved in COMSOL Multiphysics 6.1 based on Finite Element Method (FEM). The results indicate that the presence of metallic implants increases the electric field intensity, Specific Absorption Rate (SAR), and temperature within the tissues. The skin layer consistently demonstrates the highest absorption of electric field due to its proximity to the EM source and higher dielectric properties. Additionally, the absorption pattern across the different head layers is influenced by the dielectric and thermal characteristics of individual tissues. Metallic implants significantly alter the spatial distribution of hotspots in head, resulting in enhanced energy localization and deeper penetration in surrounding tissues. In several cases, SAR values exceed the safety limit (2 W/kg) recommended by the International Commission on Non-Ionizing Radiation Protection (ICNIRP). Although the temperature rise remains within safe thresholds, prolonged or repeated exposure could pose thermal risks. These findings underscore the need to consider implant presence in EM safety assessments for 5G environments.

1. Introduction

The global implementation of fifth generation (5G) wireless communication systems has ushered in a new era by providing high-speed data transmission, minimal latency, and extensive device interconnectivity. To achieve these performance metrics, 5G networks utilize a broad spectrum of radio frequencies, commonly categorized into low-band (<1 GHz), mid-band (1–6 GHz), and high-band or millimeter wave (24–100 GHz). Each frequency band offers specific trade-offs in terms of coverage, penetration depth, and data throughput. Low band 5G, with its superior propagation characteristics, ensures broad coverage and deep penetration, especially in rural areas, but is limited in data capacity. On the other end, high-band (mm Wave) offers ultra-high speeds and minimal latency but suffers from limited penetration and range, requiring dense base station infrastructure [1]. Mid-band frequencies, typically ranging from 1 to 6 GHz, strike a balance between these extremes, making them ideal for urban and suburban environments. They offer moderate-to-high speeds with better indoor penetration and reduced energy consumption, thereby forming the backbone of commercial 5G deployments globally [2,3].

Despite the performance advantages, widespread deployment of 5G technology has raised concerns regarding the biological impact of non-ionizing EM radiation, particularly on the human head, which is commonly exposed during mobile phone usage. While 5G radiation falls under non-ionizing radiation, which lacks the photon energy required to ionize atoms or directly damage DNA, concerns persist regarding its thermal effects (due to energy absorption in tissues) and non-thermal effects (such as oxidative stress or altered cellular behavior) [4–7].

* Corresponding author at: Department of Mechanical Engineering, Faculty of Engineering, Kasetsart University, 50 Ngam Wong Wan Road, Ladyaow Chatuchak, Bangkok 10900, Thailand.
E-mail address: deepshikha.b@ku.th (D. Bhargava).

https://doi.org/10.1016/j.tsep.2026.104814
Received 18 June 2025; Received in revised form 29 March 2026; Accepted 21 June 2026
Available online 22 June 2026
2451-9049/

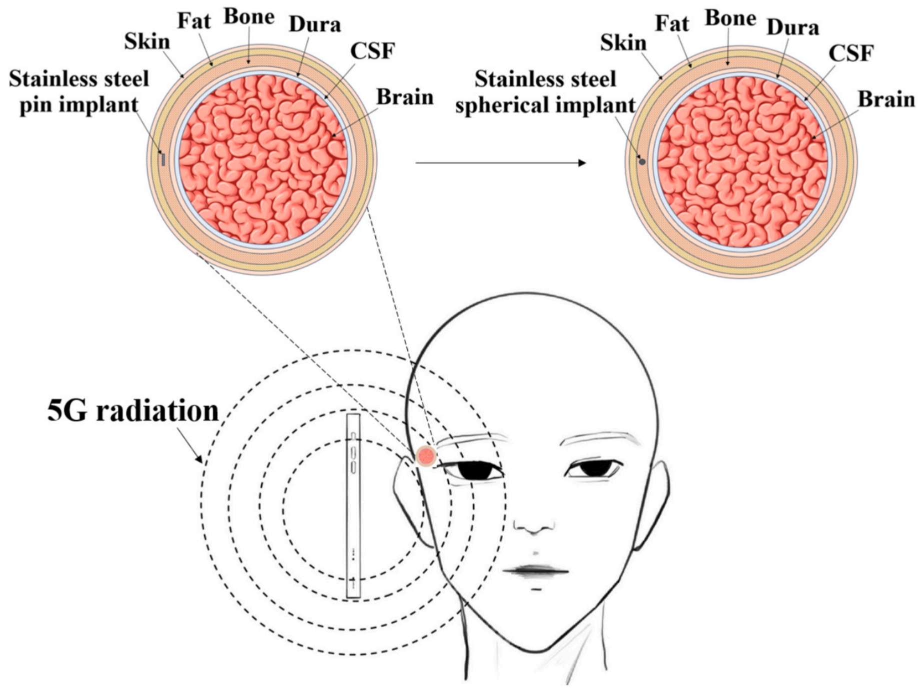

Fig. 1. Exposure of a human head with metallic implants to 5G radiation emitted by a mobile device.

These concerns become especially relevant as more people are exposed for longer durations, and as newer frequency bands are introduced into everyday environments.

To evaluate EM radiation exposure, Specific Absorption Rate (SAR) is a key metric used to quantify the rate at which energy is absorbed per unit mass of tissue. International Commission on Non-Ionizing Radiation Protection (ICNIRP) and IEEE have defined SAR limits to safeguard public health, typically 2 W/kg averaged over 10 g of tissue [8,9]. Moreover, slight temperature elevations in the brain can impact sensitive organs. While a rise of up to 3.5 °C in overall brain temperature is generally considered acceptable, an increase as small as 0.2–0.3 °C in the hypothalamus may disrupt normal thermoregulatory functions.

Several studies have investigated the interaction of EM radiation with human body. Wessapan et al. [10] exposed a two-dimensional model of the human trunk to electromagnetic radiation at 915 MHz and 2450 MHz. They found that lower frequencies (915 MHz) penetrate deeper into body tissues, while higher frequencies (2450 MHz) result in stronger EM absorption near the surface. The study also revealed that both SAR and temperature distributions depend significantly on the thermal and dielectric properties of individual tissues. Our earlier research has thoroughly investigated how EM radiation from mobile phones interacts with an adult head, child head, and human eye [11–13], We found that a child's head absorbs more radiation than an adult's under similar exposure conditions due to its smaller size and higher dielectric properties. Additionally, the voice-calling position leads to higher absorption compared to video calling and texting, primarily due to the shorter distance between the mobile phone and the head. When the human eye is exposed to EM radiation, the cornea experiences the highest absorption due to its anatomical location. Our studies also revealed that EM absorption in the head is highly dependent on factors such as device position, distance, exposure duration, and the dielectric and thermal properties of the tissues. In many cases, the computed SAR values exceeded the ICNIRP safety limits, and the associated temperature rise also surpassed biologically acceptable thresholds, emphasizing the need for further investigation and protective measures.

With the widespread daily use of the latest generation of 5G devices, particularly those operating in the mid-band frequency range, there has been growing scientific interest in understanding their potential impacts on human health, prompting numerous studies on EM exposure and biological interactions. Awada et al. [14] demonstrated that higher 5G frequencies, such as 29 GHz and 33 GHz, exhibit shallow penetration but can lead to high local SAR levels near the skin. Lwin et. al [15] investigated effect of the EM wave polarization on SAR and temperature increase in a human head model exposed to different 5G frequencies using the Finite-Difference Time-Domain (FDTD) method. They found that the SAR and resultant temperature rise within the head were influenced by both the frequency and the polarization of the incident wave. Additionally, at longer exposure durations, SAR and temperature do not exhibit a direct correlation, highlighting the need to study the effects of EM radiation on tissues over extended periods. In another similar study by Kaburcuk et. al [16] also exposed a human head to different 5G frequency from a base station. The maximum SAR and temperature were found in the eye of the head model. They also found that the SAR and temperature distribution within the human head are influenced by both the frequency of the EM field and the incident angle.

Studies also show that metallic objects near the head, such as spectacles, implants, or earrings, can increase local SAR values and disturb the thermal balance of tissues [17,18]. In our previous work [19], we studied how the presence of metal objects (different metal jewelry and spectacles) outside the head can influence the EM absorption in the tissues. It was found that in some cases the presence of these metal objects further increases the EM absorption in human head. Metallic implants within the human body, such as cranial plates, pins, or electrodes, can notably alter the distribution of electromagnetic field, potentially leading to localized increases in SAR and tissue temperature [20–23]. A recent study by Wessapan et. al [20] showed that metallic implants in human skin significantly alter the EM field distribution, leading to localized heating around the implant site. The extent of heating depends on the implant's material, geometry, and depth within the tissue. This underscores the importance of evaluating implant safety under RF exposure, especially in the context of modern wireless technologies.

Given the growing global reliance on mid-band 5G technology and the increasing prevalence of individuals with cranial implants, it is essential to evaluate how these frequencies interact with biological

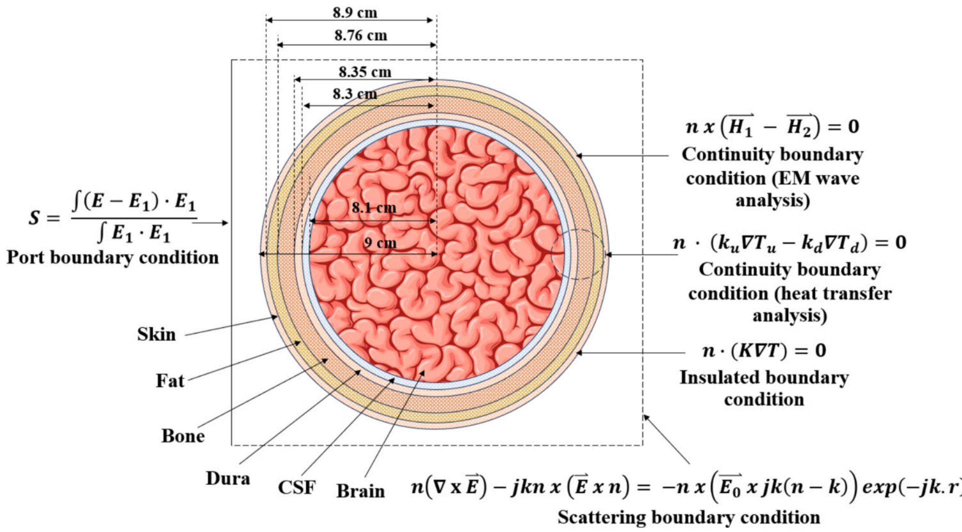

Fig. 2. Mathematical model of human head exposed to 5G radiation.

tissues in the presence of metal. This is the first study to systematically analyze the effects of mid-band 5G radiation on clinically relevant cranial metallic implants (stainless steel 410) of different shapes in a six-layer heterogeneous head model. This approach addresses an important gap in existing literature, as most previous studies have primarily focused on external metallic objects or simplified single-layer tissue models or have not considered the effects of mid-band 5G radiation. This study uses a 2D head model which significantly reduces computational cost and time, as solving a full 3D model across multiple frequencies and implant geometries would be highly time-consuming and computationally intensive. However, a numerical validation study is conducted to ensure the reliability of the proposed model and method, and the obtained results are compared with those reported in the literature.

The objective of this study is to assess SAR and temperature rise in a 2D anatomical human head model exposed to mid-band 5G frequencies (2.6, 3.6, 4.4, and 6 GHz). A stainless steel 410 implant modelled as a pin and a sphere, is embedded within the cranial bone layer. The model includes six layers- skin, fat, bone, dura, cerebrospinal fluid (CSF), and brain. FEM is used to solve Maxwell's equations for EM wave propagation and Pennes' bioheat equation for thermal analysis. The simulation compares results with and without the implant, evaluates SAR against ICNIRP safety limits, and investigates whether the observed temperature elevations present potential health risks. The present study addresses a critical gap in current 5G safety research by focusing on individuals with metallic cranial implants, thereby contributing valuable insights for regulatory development and public health assurance in the age of 5G.

The rest of the paper is organized as follows: Section 2 (Problem Formulation) describes each part of the model and the parameters used in the study. Section 3 (Mathematical Model) explains the coupled mathematical model of EM wave and bioheat transfer used in the study. Section 4 (Results) presents the results on the effects of implants on radiation absorption in the tissues. Section 5 (Discussion) discusses the key findings, future work and limitations of the study, and finally, Section 6 (Conclusion) summarizes the findings of the study.

2. Problem formulation

Due to ethical constraints associated with exposing real humans to EM radiation, this study employs a 2D heterogeneous human head model to investigate the interaction of 5G EM radiation with head tissues in presence of the cranial implants. The model comprises six concentric tissue layers: skin, fat, bone, dura, cerebrospinal fluid (CSF), and brain. The effect of metallic implants of varying shapes on the absorption of EM radiation is analyzed. Fig. 1 illustrates a realistic scenario in which a human head is exposed to 5G radiation coming during mobile phone usage. Two geometries of the metallic implant are considered within the bone layer: a cylindrical pin (0.5 mm × 5 mm) and a sphere (radius = 1 mm). The implant material is stainless steel 410, characterized by an electrical conductivity (σ) of 1.74 × 10^6 S/m, relative permeability (μ_r) of 700, density (ρ) of 7880 kg/m^3, thermal conductivity (k) of 25 W/m°C, and specific heat capacity (C_p) of 460 J/kg°C [20]. Fig. 2 presents the dimensions of the head model and its respective tissue layers. The radii of the skin, fat, bone, dura, CSF, and brain layers are 9.0 cm, 8.9 cm, 8.76 cm, 8.35 cm, 8.3 cm, and 8.1 cm, respectively, taken from [15]. All tissues are assumed to be isotropic and homogeneous. The 5G EM source is positioned 1 cm away from the head surface and operates at frequencies of 2.6 GHz, 3.6 GHz, 4.4 GHz, and 6 GHz, each with a radiated power of 1 W. The dielectric and thermal properties of each tissue layer are taken from Tables 1 [16,24], and 2 [15] and are assumed to remain constant throughout the simulation. The 5G radiation propagates through air and incident on the head model, where it gets absorbed across the tissue layers. The absorbed EM energy is subsequently converted into thermal energy, leading to a rise in tissue temperature. To simulate this phenomenon, the FEM in COMSOL™ Multiphysics is employed to solve a coupled EM wave and bioheat transfer model [11,12,25,26].

Table 1
Dielectric properties of tissues for different 5G frequencies.[16,24].

Tissues	2.6 GHz		3.6 GHz		4.4 GHz		6 GHz	
	σ(S/m)	ε	σ(S/m)	ε	σ(S/m)	ε	σ(S/m)	ε
Skin	1.54	37.8	2.09	36.9	2.61	36.3	3.89	34.9
Fat	0.11	5.26	0.16	5.16	0.20	5.09	0.30	4.94
Bone	0.42	11.3	0.63	10.7	0.82	10.3	1.20	9.59
Dura	1.76	41.8	2.44	40.6	3.07	39.6	4.50	37.6
CSF	3.60	66.0	4.69	64.4	5.73	63.0	8.16	60.1
Brain	2.20	44.5	2.95	43	3.63	41.9	5.20	39.7

3. Mathematical model

2D EM wave in Transverse Electric (TE) mode radiates from the left side, as shown in Fig. 2, and incident on the head model. To simplify the numerical analysis and computational complexity following assumptions are made:

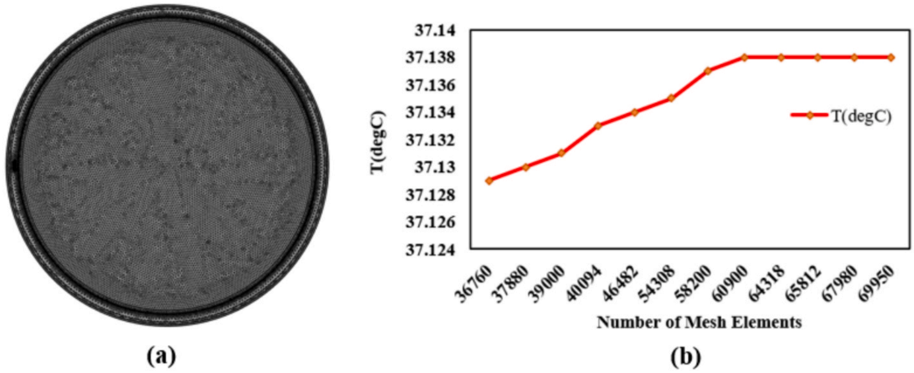

Fig. 3. (a) 2D FEM mesh head model and (b) mesh convergence graph of the head model.

1. The numerical analysis of EM wave interaction with the head model is considered in 2D.
2. The head model is truncated by scattering boundary condition.
3. The dielectric and thermal properties of the tissues are constant throughout the analysis.
4. There is no chemical reactions and phase change of the substances in the head model.
5. The heat transfer is only considered in the head model and not in the surroundings.
6. The initial temperature of the head model is assumed to be uniform at 37 °C.

3.1. Electromagnetic wave propagation analysis

Maxwell's equation are solved by FEM to calculate the propagation of EM wave in the surrounding as well as inside the head model [27]. Eq. (1) shows the simplified version of the Maxwell's equation in TE mode

$$\nabla \times \left(\frac{1}{\mu_r}\nabla \times \mathrm{E}\right) - k_0^2\left(\varepsilon_r - \frac{j\sigma}{\omega\varepsilon_0}\right)E = 0 \quad (1)$$

where E is total electric field (V/m), μ_r is the relative magnetic permeability, ε_r is the relative dielectric constant, ε_0 is the permittivity of free space 8.8542×10^{-12} (F/m), σ is the electric conductivity (S/m), and k_0 is the free space wave number (m^{-1}).

3.1.1. Port boundary condition

On the left side of the numerical model, a TE wave propagation port with a defined power density is applied, as shown in Fig. 2. Different 5G frequencies are radiated from the port boundary with a radiated power of 1 W [19]

$$\mathrm{S} = \frac{\int (\mathrm{E} - \mathrm{E}_1) \bullet \mathrm{E}_1}{\int \mathrm{E}_1 \bullet \mathrm{E}_1} \quad (2)$$

where E is total electric field (V/m), and E_1 is reference field

3.1.2. Continuity boundary condition

Continuity boundary condition is applied at the interfaces between different layers within the head model (tissue-to-tissue) as well as between the external environment and the head (air-to-tissue) [11]

$$\mathrm{n} \times \left(\vec{\mathrm{H}}_1 - \vec{\mathrm{H}}_2\right) = 0 \quad (3)$$

3.1.3. Scattering boundary condition

To simplify the numerical analysis and reduce computational time, the 2D head model is truncated using scattering boundary conditions, shown in Fig. 2. These boundary conditions absorb outgoing and reflected EM waves, preventing artificial reflections from the edges of the simulation domain. This ensures that the computational results more accurately represent an open and infinite environment, thereby improving the realism and stability of the simulation [27]

$$n\left(\nabla \times \vec{E}\right) - jkn \times \left(\vec{E} \times n\right) = -nx\left(\vec{E_0} \times jk(n-k)\right)\exp(-jk \bullet r) \quad (4)$$

where k is the wave number (m^{-1}), σ is the electric conductivity (S/m), n is the normal vector j is $\sqrt{-1}$, and ($\vec{E_0}$) is the incident plane wave (V/m).

3.2. Specific absorption rate (SAR)

The EM wave, propagating in the TE mode, is incident upon the head model, where its energy is absorbed by the head tissues. The absorbed energy is quantified in terms of the Specific Absorption Rate (SAR), which represents the rate of power dissipation per unit mass of the tissue. Mathematically, SAR is defined as the power absorbed per kilogram of tissue and is expressed using the following equation [11]

$$\mathrm{SAR} = \frac{\sigma}{\rho}|E|^2 \quad (5)$$

where ρ is the tissue density $(\mathrm{kg/m^3})$.

3.3. Bioheat transfer

The absorbed EM radiation in the tissue layers then converts into thermal energy leading to increase in the overall temperature of the head. To calculate the temperature, increase in the different layers of the head tissues, Pennes' bioheat equation is used. The initial temperature of the head model is set to 37 °C [15,19,28].

$$\rho C\frac{\partial T}{\partial t} = \nabla \bullet (k\nabla T) + b(T_b - T) + Q_{met} + Q_{ext} \quad (6)$$

where ρ is the tissue density $(\mathrm{kg/m^3})$, C is the heat capacity of tissue $(\mathrm{J/kgK})$, k is the thermal conductivity of tissue (W/mK), T is the tissue temperature (°C), $\mathrm{T_b}$ is the temperature of blood (°C), b is the term related to blood flow ($\mathrm{W/m^3}$ °C), and $\mathrm{Q_{ext}}$ is the external heat source $\left(\frac{\mathrm{W}^3}{\mathrm{m}}\right)$.

3.3.1. Insulated boundary condition

Insulated boundary condition is applied on the outer layer of the head model which indicates that the heat transfer only occurs in the head model and not in the outer surrounding [11].

$$n \bullet (K\nabla T) = 0 \quad (7)$$

3.4. Numerical implementation

The 2D head model with the implant embedded in the bone layer is

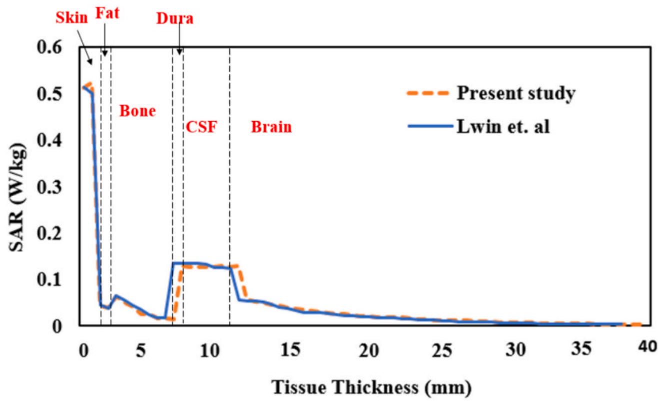

Fig. 4. Numerical validation between present study and Lwin et al [15].

modeled and exposed to 5G EM source. Due to the use of a 2D model, the computational time is significantly reduced. However, mesh convergence analysis and numerical validation (Section 4.1) have been conducted to ensure the accuracy and reliability of the results. A coupled model of EM wave and bioheat transfer is used to investigate the electric field, specific absorption rate (SAR), and temperature distribution in the head model. Maxwell's equations were solved using the EM wave module to obtain the electric field distribution and the resulting volumetric heat generation within the tissues. This heat source term was then used in the bioheat transfer module, where Pennes' bioheat equation was solved to determine the temperature distribution within the head model. The coupled model is solved using FEM. The computational domain was discretized using triangular elements, with local mesh refinement applied in sensitive regions, particularly near the metallic implant, to ensure improved numerical accuracy. The study employs an implicit time step scheme to solve the electric field and temperature field. Fig. 3 (a) shows the meshed head model, while Fig. 3 (b) presents the mesh convergence study for the maximum temperature in the head model with a pin implant at a frequency of 3.6 GHz (discussed in detail in section 4.4). As observed, the temperature values converge when the mesh contains approximately 60,000 elements for 37.138 °C, indicating that the numerical solution becomes independent of further mesh refinement. This confirms that the chosen mesh density provides accurate and stable simulation results.

4. Results

4.1. Numerical validation

Since it is unethical to expose humans to radiation, validating the numerical results through experiments is very challenging. Therefore, to assess the reliability of the proposed numerical methods, a numerical validation is performed by replicating the numerical work of Lwin et al. [15] step by step. The head model used in the present study for the numerical validation has the same dimensions as that of Lwin et al. [15]. Following their methodology, the head model was exposed to a 5G EM source at a frequency of 3.35 GHz and radiated power of 1 W. The 5G radiation incident on the head model is absorbed by the tissues. The absorbed EM field in the tissues is used to calculate the SAR, and the resulting values in different head layers are compared with those reported by Lwin et al. [15]. Fig. 4 shows the comparison of SAR values between the present study and Lwin et al. Highest SAR in both cases are found in the skin layer of the head. Apart from that, SAR values in all head tissues were very similar in both studies. This close agreement demonstrates that the current method effectively reproduces the original findings, thereby confirming its accuracy.

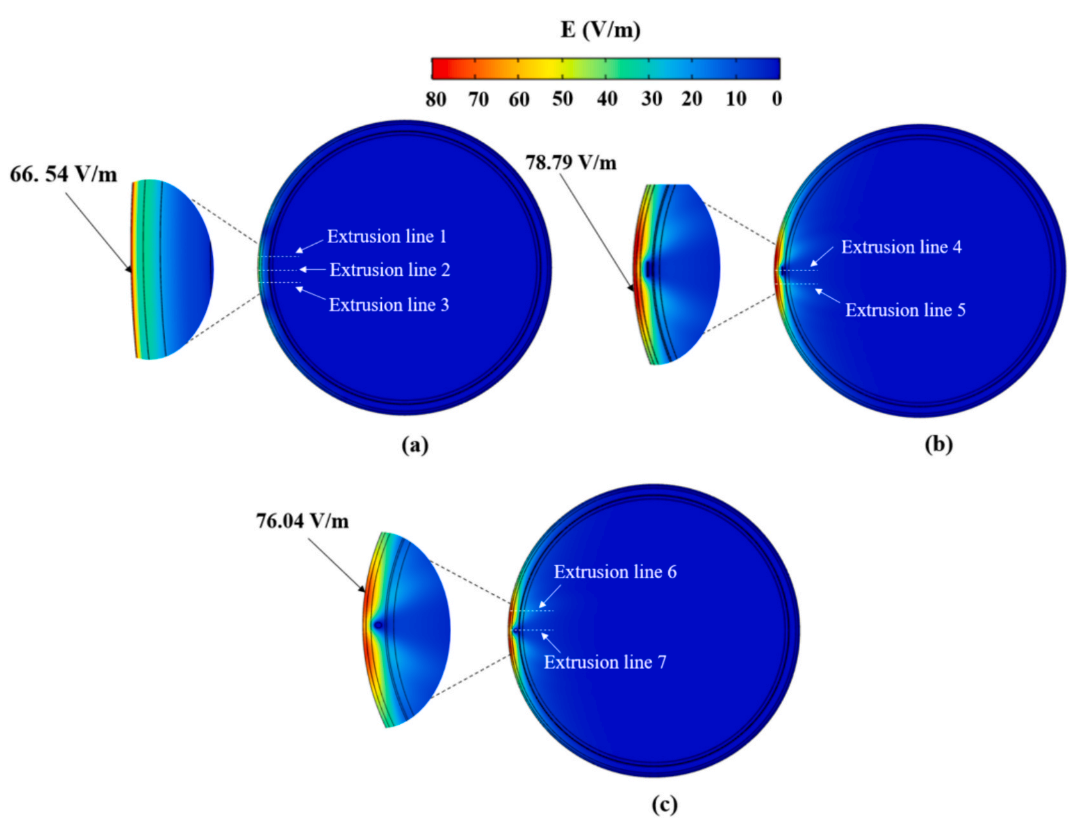

Fig. 5. Max value of electric field in the head for 3.6 GHz frequency for the cases of: (a) absence of implant, (b) presence of the pin-shaped metal implant, and (c) presence of the sphere-shaped metal implant.

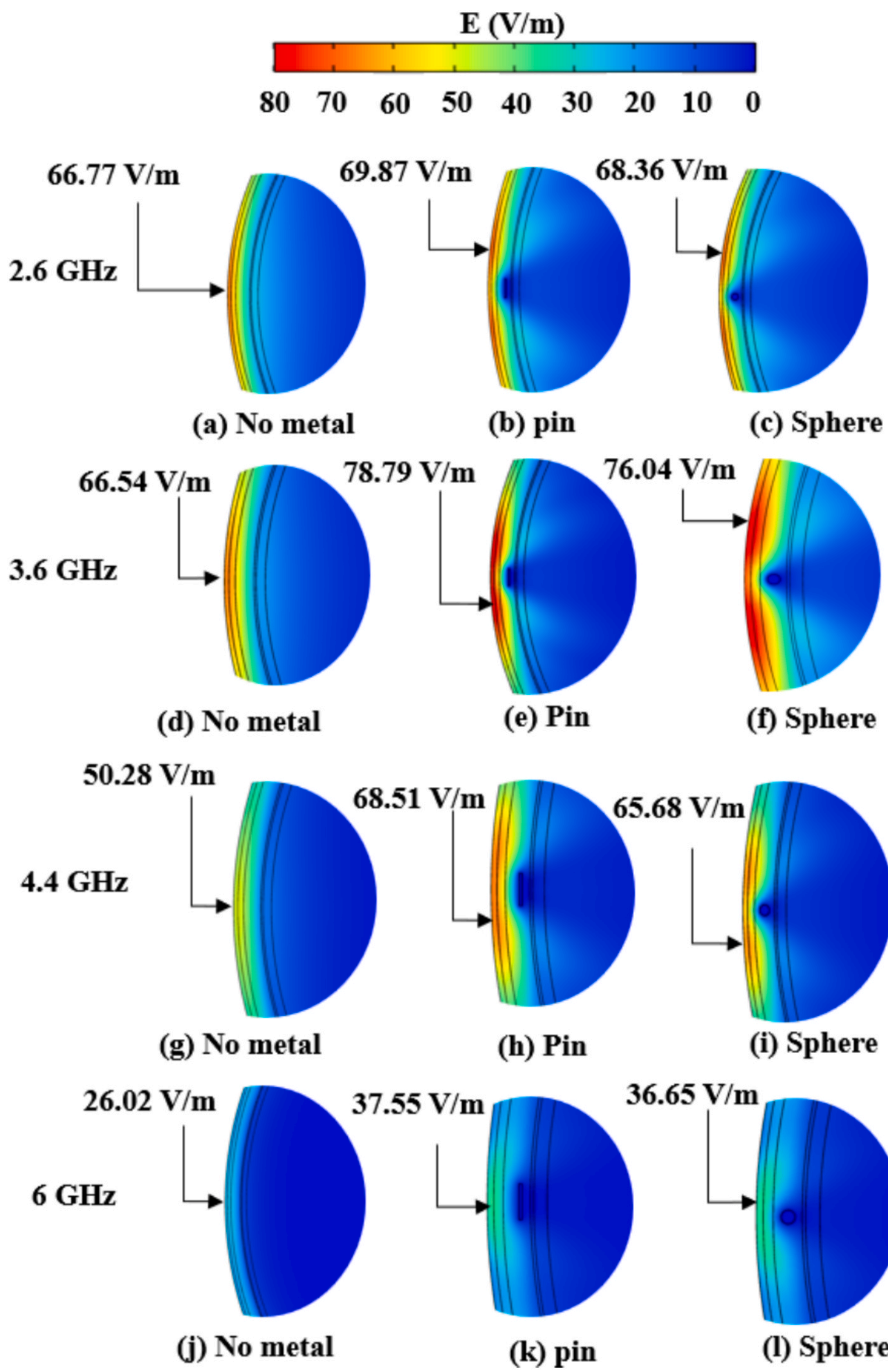

Fig. 6. Electric field distribution in the head model in the presence and absence of the metal implants at different 5G frequencies.

4.2. Electric field distribution in the head

The electric field distribution within the human head under exposure to 5G frequencies is computed and analysed in this study. EM waves are generated using a port boundary condition, as presented in Fig. 2. These waves propagate through free space and are incident upon the head model, where they are subsequently absorbed by various tissue layers. The metal implant used in the simulations is a stainless steel 410 and is embedded within the bone layer. Simulations are conducted at four different 5G frequencies, 2.6 GHz, 3.6 GHz, 4.4 GHz, and 6 GHz, with a radiated power of 1 W. The results indicate that the presence of a metal implant significantly increases the electric field absorption within the head tissues for all tested frequencies, with the highest absorption observed at 3.6 GHz. Fig. 5 presents the maximum electric field distribution in the head model at 3.6 GHz for three configurations: (a) absence of implant, (b) presence of a pin-shaped implant, and (c) presence of a sphere-shaped implant. As shown, the highest electric field intensity is found in the presence of the pin-shaped implant (78.79 V/m), followed by the sphere-shaped implant (76.04 V/m), and the lowest in the absence of any implant (66.54 V/m).

Fig. 6 shows a magnified view of the electric field distribution at the front section of the head model across all examined 5G frequencies in the presence and absence of the metal implants. As can be seen in all cases the electric field in the head is higher in presence of the metal implant. Additionally, in all cases, the skin layer exhibits the highest electric field absorption. This behaviour is attributed to the skin being the outermost

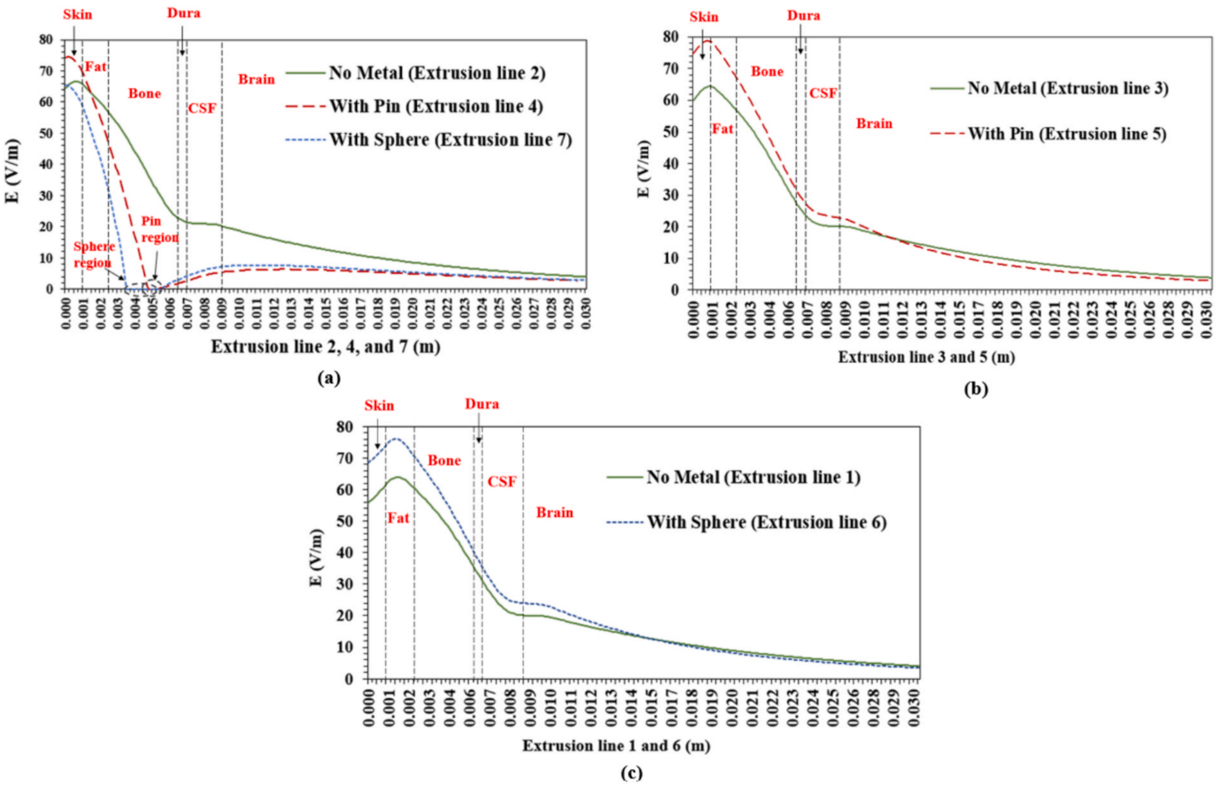

Fig. 7. Comparison of electric field absorption in head layers at 3.6 GHz frequency and 1 W radiated power along the extrusion lines: (a) extrusion lines 2, 4 and 7, (b) extrusion lines 3 and 5, and (c) extrusion line 1 and 6.

layer and hence in closest proximity to the EM source. Furthermore, the relatively higher dielectric properties of skin (Table 1) compared to fat and bone further contribute to greater energy absorption, in accordance with the governing relation (Eq. (1). The location of the electric field hotspot also exhibits notable differences depending on the presence and shape of the metal implant. In the absence of the implant, the hotspot consistently appears at the front centre of the head model. However, in the presence of a pin or sphere-shaped implant, the hotspot region is observed to shift either upward or downward relative to its original position. It is also observed that the EM field penetrates deeper into the underlying tissue layers in the presence of implants. This shifting and deepening of the hotspot suggest that the metal implant alters the EM field distribution within the head model.

Since the maximum electric field intensity is observed at 3.6 GHz for all three scenarios, a comparative analysis of the electric field distribution across the head layers was conducted. To facilitate this analysis, specific extrusion lines were defined within the head models, as depicted in Fig. 5. Given that the hotspot regions differ depending on the presence and type of metal implant, direct comparison along identical extrusion lines is not feasible. Therefore, different extrusion lines were selected based on the location of the maximum electric field for each respective case. Extrusion lines 2, 4, and 7 correspond to the central region of the head model, where the peak electric field is observed in the absence of a metallic implant (Fig. 5a). Extrusion line 2 represents the no-implant scenario, while lines 4 and 7 were positioned at the same coordinates in the models with the pin- and sphere-shaped implants, respectively, to assess the comparative influence of the implants at that location. Extrusion lines 3 and 5 are drawn slightly below the center of the model, where the maximum field occurs in the presence of the pin-shaped implant (Fig. 5b). Lastly, extrusion lines 1 and 6 represent the region of highest field intensity in the presence of the sphere-shaped implant (Fig. 5c).

Fig. 7 presents the electric field distributions along these extrusion lines. Fig. 7(a) shows a comparison along lines 2, 4, and 7. The results indicate that the presence of metallic implants leads to increased electric field absorption in the skin layer. The peak field occurs in the skin for both implant scenarios. However, a sharp decline in the electric field is observed at the implant locations, marked by circles in Fig. 7(a), indicating local redistribution and absorption by the metallic materials. Consequently, the electric field in the deeper tissues (such as the brain) is reduced compared to the no-metal condition (line 2), as also evidenced by the spatial field distributions in Fig. 5. Fig. 7(b) compares electric field values along extrusion lines 3 and 5, which intersect the maximum field region in the presence of the pin-shaped implant. The field intensity is initially higher in the presence of the implant (line 5). However, as the field propagates through the brain layers, the difference between the two cases diminishes, and the values converge, indicating that the pin-shaped implant's influence is more pronounced near the surface and diminishes with depth. Fig. 7(c) presents the comparison along extrusion lines 1 and 6, located at the maximum field region for the sphere-shaped implant. A similar behaviour is observed, where the presence of the sphere increases the electric field intensity near the surface (line 6), particularly in the skin and fat layers. As the field penetrates deeper into the tissue, the values along line 6 gradually decrease and approach those of the no-metal case (line 1). Overall, this analysis confirms that metal implants significantly alter the local spatial distribution of the electric field within the head. Depending on the type and position of the implant, local field intensities can either increase or decrease, particularly affecting the superficial layers while having diminishing influence in deeper tissues. This behaviour of electric field absorption in different head tissue layers is very similar to the published work of [29].

4.3. SAR distribution in the head

This section presents a comparative analysis of the SAR distribution in the human head model in presence and absence of metal implants. The SAR values were calculated using the electric field from Section 4.2

Table 2
Thermal properties of tissues [11,15].

Tissues	C_p (J/ kg °C)	K (W/m °C)	ρ(kg/m^3)	b(W/m^3 °C)
Skin	3600	0.42	1010	9100
Fat	3000	0.25	920	1700
Bone	3100	0.39	1810	3300
Dura	3600	0.5	1010	9100
CSF	4000	0.62	1010	0
Brain	3650	0.535	1040	40,000

and the dielectric and thermal properties of the tissues provided in Table 1 and 2, based on Eq. (5). It is observed that the SAR distribution closely follows the pattern of electric field absorption described in Section 4.2 with the highest value of SAR to be found at 3.6 GHz frequency in all cases. Fig. 8 shows the max SAR at 3.6 GHz frequency in the head model for all three cases: (a) absence of implant, (c) presence of pin implant, and (c) presence of sphere implant. Similar to section 4.2 the highest value of SAR is found at pin implant 6.42 W/kg, followed by sphere implant 5.98 W/kg, and absence of implant 4.58 W/kg. It is also seen that the SAR hotspot region shifts in position due to the presence of the implant.

However, the penetration depth of the SAR hotspot is observed to be shallower than that of the electric field, indicating that SAR is more concentrated near the outer layers of tissue. Fig. 9 shows the magnified front view of SAR distribution in head models across all frequencies in all cases. The highest SAR values are consistently found in the skin layer, owing to its proximity to the EM source and its relatively high dielectric properties. Skin has higher value of dielectric and thermal properties than the fat and bone layers. Furthermore, the presence of a metallic implant, whether pin- or sphere-shaped, results in higher SAR values compared to the no-implant scenario across all frequencies. When compared against the ICNIRP safety guideline for local exposure (maximum 2 W/kg), it is evident that the SAR values exceed the permissible limit in all cases, except at 6 GHz without the implant, where the SAR is 1.29 W/kg. Furthermore, the distribution of SAR in the head layers is also studied and compared along different extrusion lines, as shown in Fig. 8. Extrusion lines 2, 4 and 7 are located at the centre of the head model where the highest value of SAR is found for the case of absence of implant (extrusion line 2), while extrusion lines 3 and 5 are positioned slightly below, where the highest value of SAR is found for the presence of the pin implant (extrusion line 5), and lastly extrusion lines 1 and 6 are positioned slightly above from the centre where the maximum value of SAR is found for the sphere implant (extrusion line 6).

Fig. 10 shows the comparison of SAR distribution in the head layers along these extrusion lines. It is observed that the SAR distribution follows the similar pattern as the electric field distribution in Fig. 7, with always higher values in the skin layer of the head. Fig. 10(a) shows the SAR distribution along extrusion lines 2, 4 and 7. The presence of the metal implant leads to a higher SAR in the skin layer and a sharp drop within the implant region. After this region, the SAR for extrusion line 4 (with pin implant) and 7 (with sphere implant) becomes consistently lower than that for extrusion line 2 (no implant). Similarly, Fig. 10 (b) presents the SAR comparison along extrusion lines 3 and 5. In this case, the SAR along extrusion line 5 (with the pin implant) is consistently higher for all head layers up to the brain layer, and then slightly lower than that along extrusion line 3 (no metal) deeper in the brain tissue. Fig. 10 (c) shows the SAR comparison along extrusion line 1 and 6. The presence of sphere implant (extrusion line 6) also leads to higher value of SAR in the head layers, and in the brain layer the SAR also goes down below the no- implant case (extrusion line 1). It is also observed that the highest SAR are in skin and CSF layers which are in good agreement with the published work [15,29,30].

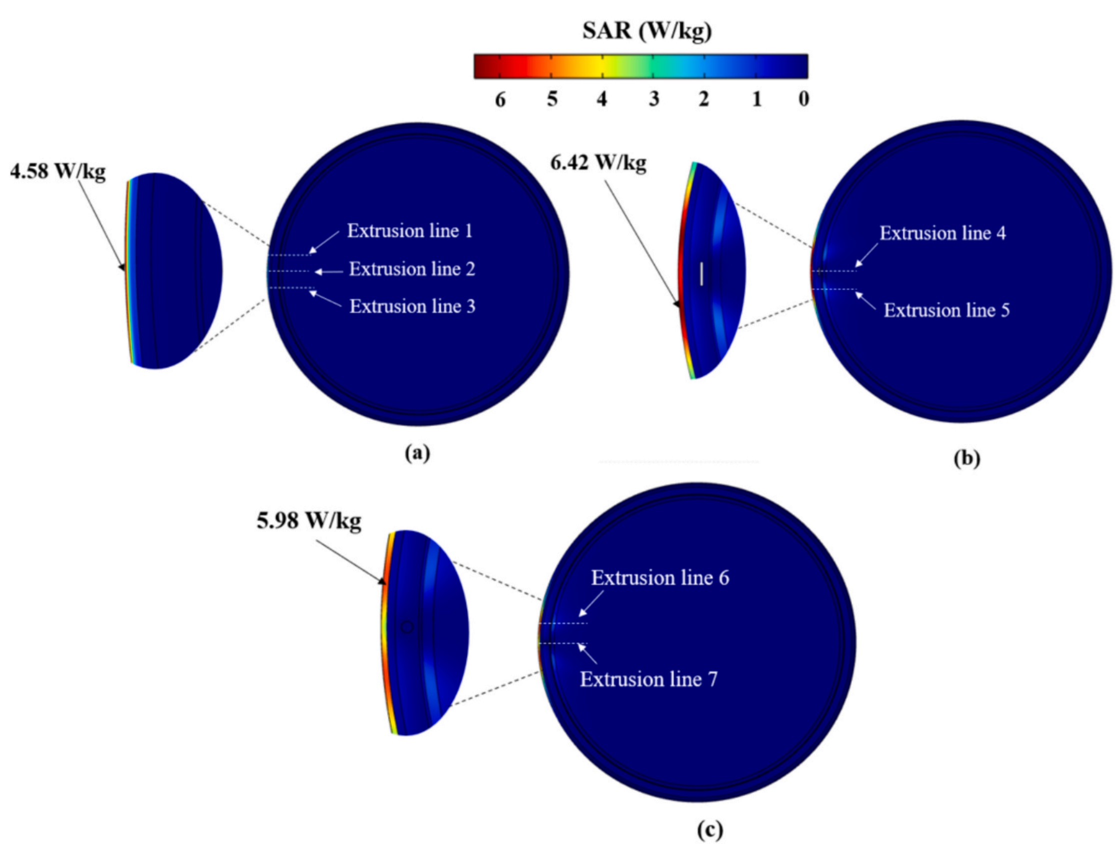

Fig. 8. Maximum value of SAR found at 3.6 GHz frequency for three cases: (a) absence of implant, (b) presence of pin implant, and (c) presence of sphere shaped implant.

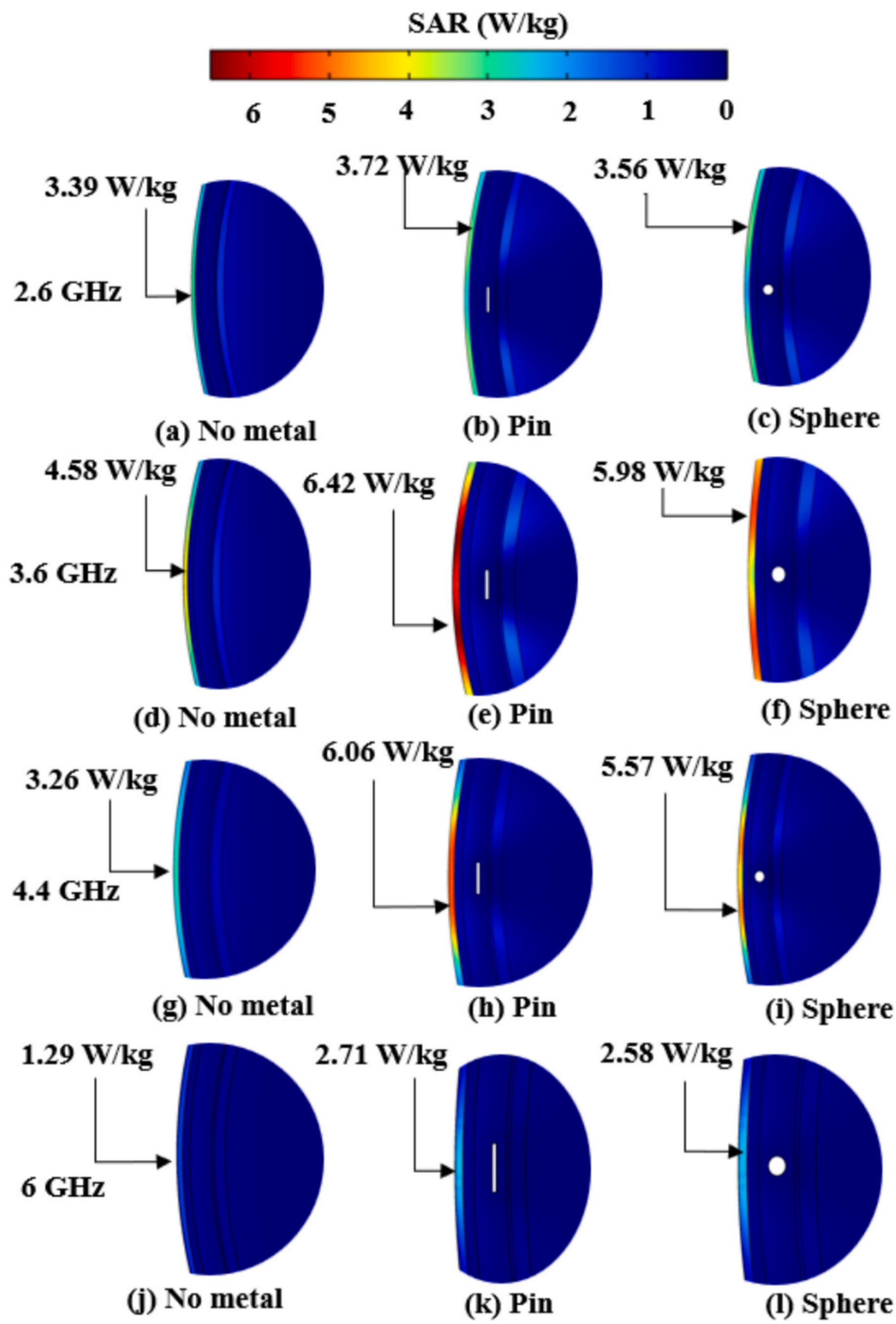

Fig. 9. SAR distribution in the head model in the presence and absence of the metal implants at different 5G frequencies.

4.4. Temperature distribution in the head

This section presents the temperature distribution in head tissues exposed to 5G EM radiation at various frequencies, considering both the presence and absence of metallic implants over an exposure duration of 30 minutes. The absorbed electric field energy changes into thermal energy increasing the overall temperature of the head model. The obtained heat generation term from Eq. (1) is used to calculate the temperature increase in the head tissues. This temperature increase is calculated using Pennes' bio-heat equation (Eq. (6). The initial temperature of the head model is set at 37 °C. Since the focus of this study is the internal temperature distribution within the head model, the ambient temperature is assumed to be equal to the body temperature (37 °C). Similar to the electric field and SAR results, the highest temperature in the head model is also observed at the 3.6 GHz frequency for all three cases, as shown in Fig. 11. The maximum temperature is recorded in the presence of the pin-shaped implant (37.138 °C), followed by the sphere-shaped implant (37.127 °C), and the lowest temperature is observed in the case without any implant (37.111 °C).

Fig. 12 presents a magnified view of the temperature distribution across all frequencies, highlighting the shift in hotspot regions. The results show that the overall temperature increase remains modest across all configurations, with maximum temperatures ranging from 37.035 °C to 37.138 °C. However, consistently higher temperatures are observed in the presence of metallic implants (either pin- or sphere-shaped) compared to the no-implant scenario. This increase is attributed to the enhanced local absorption of EM energy due to field perturbations introduced by the metallic implants, as discussed in the electric field and

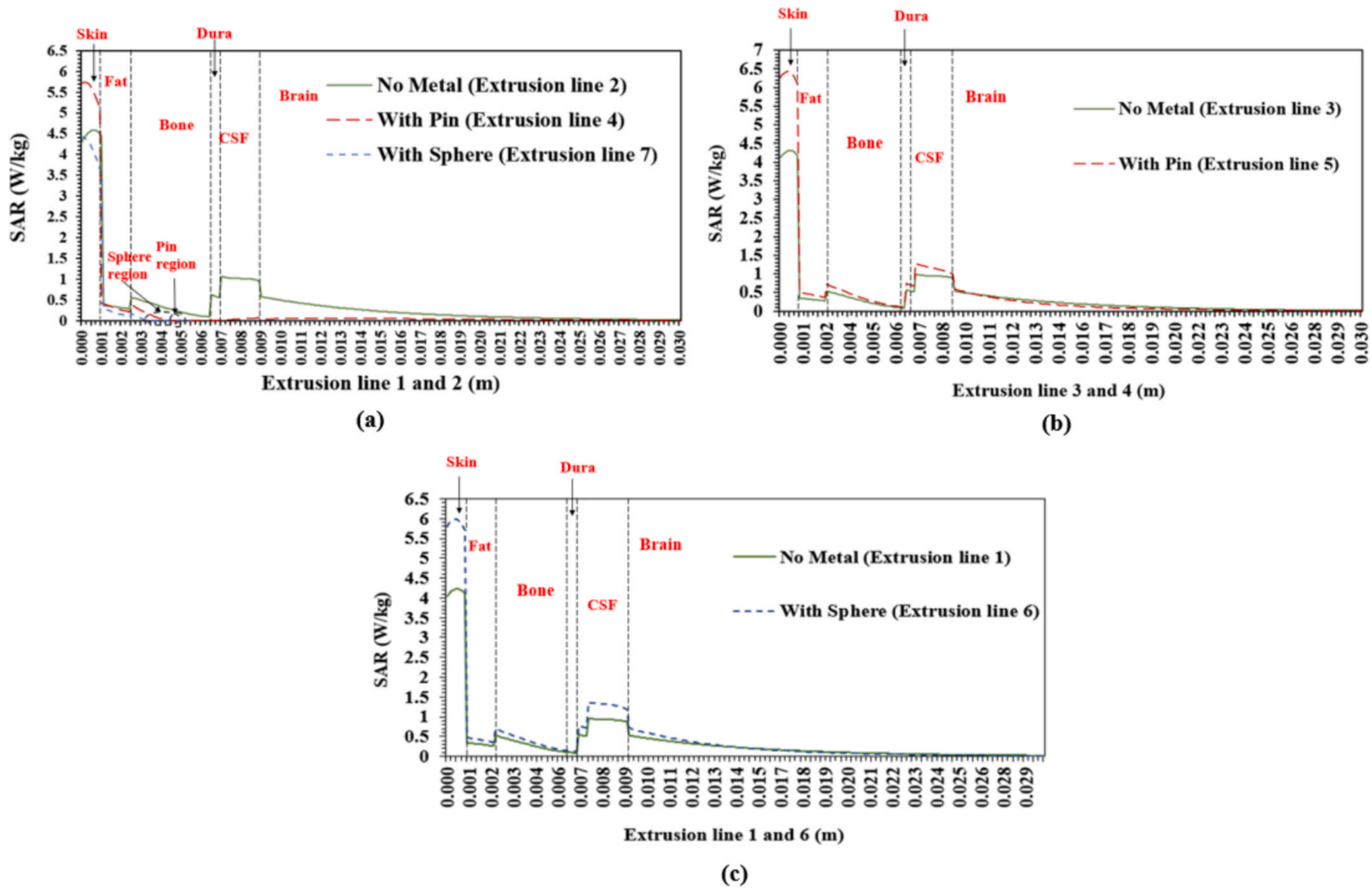

Fig. 10. Comparison of SAR in head layers at 3.6 GHz frequency and 1 W power along the extrusion lines: (a) extrusion lines 2,4 and 7, (b) extrusion lines 3 and 5, and (c) extrusion line 1 and 6.

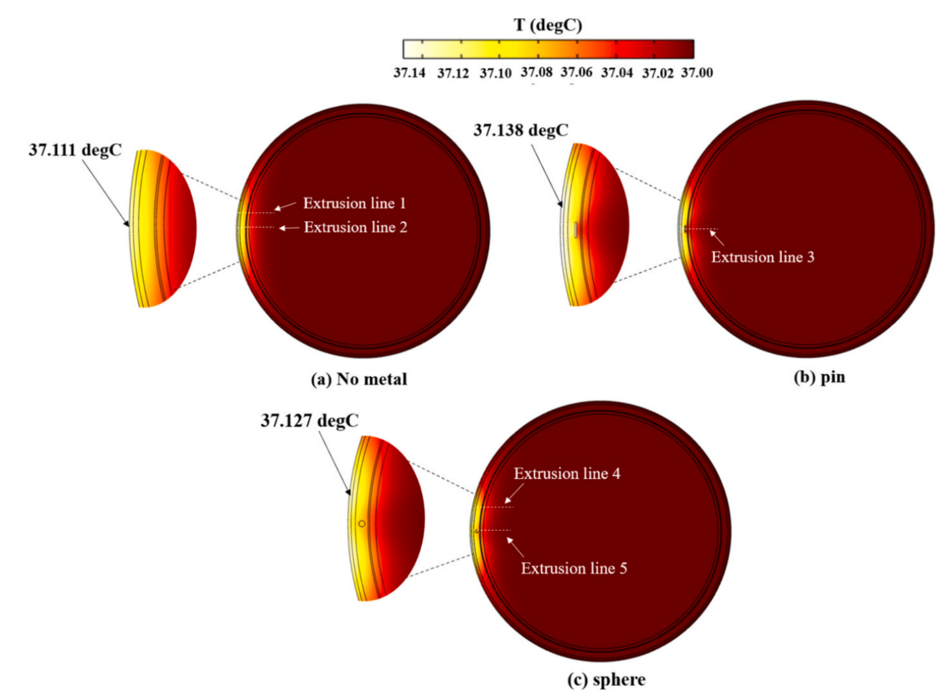

Fig. 11. Max value of temperature increase in absence and presence of the pin-shaped metal implant at 3.6 GHz frequency.

SAR analyses.

Dielectric and thermal properties listed in Tables 1, and 2 play a crucial role in determining the extent of EM radiation absorption and the resultant temperature rise within each tissue. In all cases, the skin layer

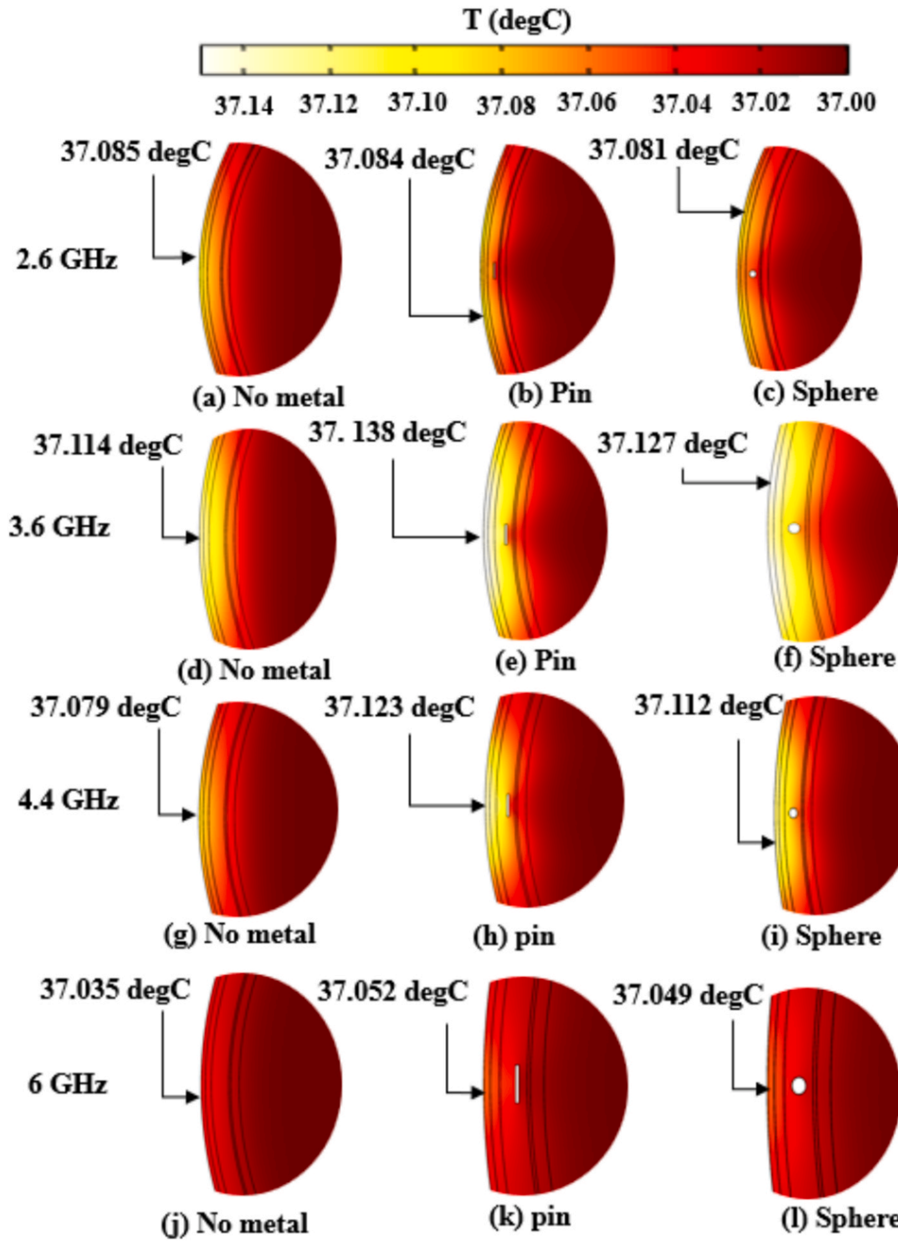

Fig. 12. Temperature distribution in the head model in the presence and absence of the metal implants at different 5G frequencies.

exhibits the highest temperature elevation due to its close proximity to the EM source and its relatively high absorption characteristics. Additionally, the skin has the highest blood perfusion rate (Table 2), which facilitates more efficient heat dissipation. The cerebrospinal fluid (CSF) layer, being a liquid medium, also aids in rapid heat transfer, contributing to a more distributed and moderated temperature profile in surrounding tissues. Although the temperature increases observed in Fig. 12 remain within accepted safety limits for short-term exposure, prolonged or repeated exposure, particularly in the presence of metallic implants, may lead to tissue temperature rises exceeding the recommended safety threshold of 3.5 °C above baseline, posing potential health risks.

Fig. 13 compares the temperature distribution along different extrusion lines at 3.6 GHz, the frequency yielding the highest temperature rise, as previously discussed. These extrusion lines are positioned where the maximum temperature values are observed in the absence and presence of metallic implants (Extrusion lines shown in Fig. 11). Fig. 13 (a) presents the comparison along extrusion lines 2 (no implant), 3 (pin implant), and 5 (sphere implant), corresponding to the location of maximum temperature in the absence of metal. It is observed that the temperature along lines 3 and 5 is initially higher than that of line 2 in the outer tissue layers. However, a sudden temperature drop occurs at the location of the metallic implant in the bone layer. Beyond this point, the temperature remains lower than that of the no-implant case (line 2). Fig. 13 (b) compares extrusion lines 2 and 3 at the location where the maximum temperature is observed in the presence of the pin implant. As can be seen, the temperature is higher in the presence of the pin until it reaches the implant location, where it sharply drops, followed by a lower temperature profile compared to the no-implant scenario. Fig. 13 (c) shows the temperature comparison along extrusion lines 1 (no implant) and 4 (sphere implant), drawn at the position of peak temperature for the sphere implant case. The temperature remains higher in the presence of the sphere implant up to the brain region, after which both profiles converge. These results indicate that while overall thermal effects remain within safe limits, metallic implants significantly affect the local heating pattern. Their influence on spatial temperature

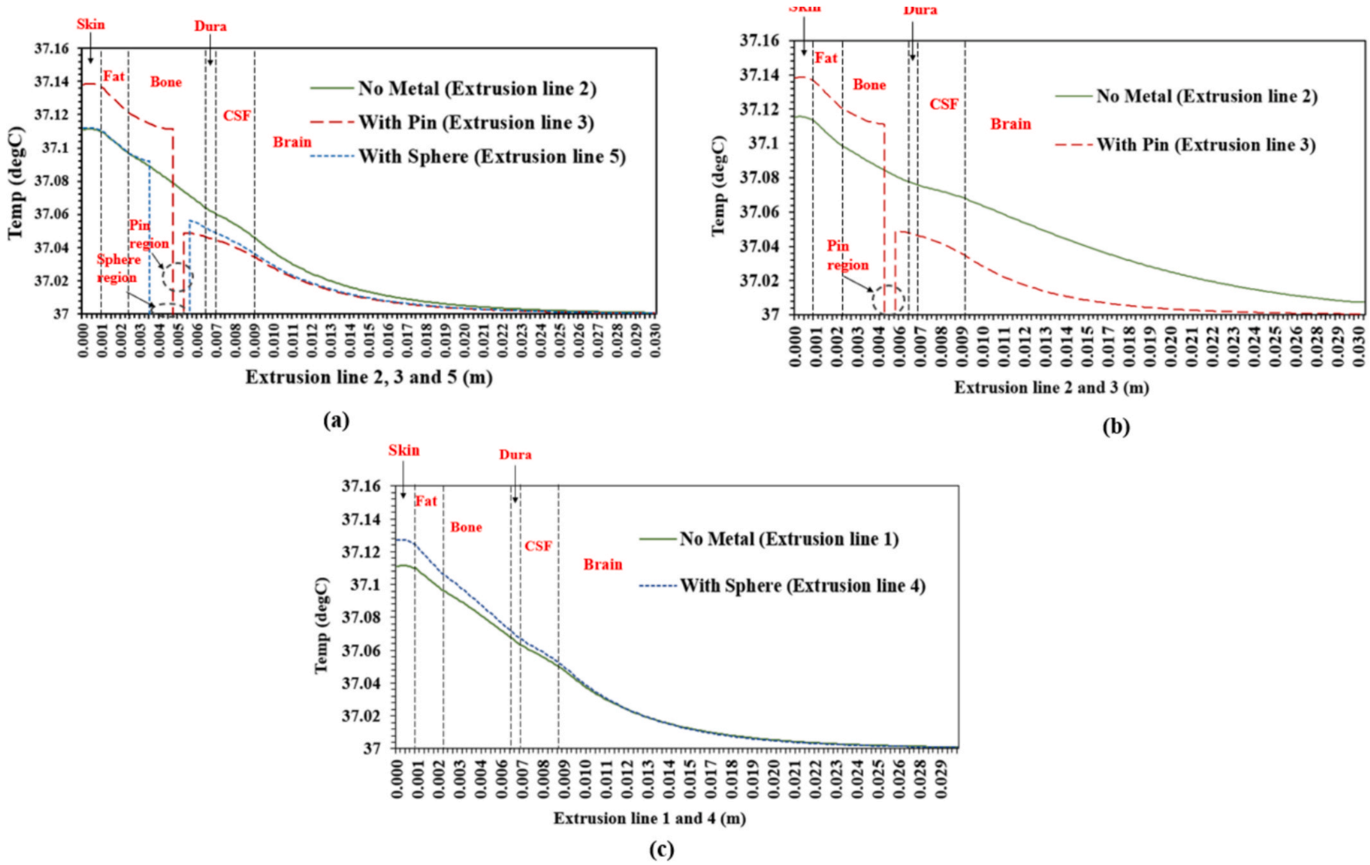

Fig. 13. Comparison of temperature increase in head layers at 3.6 GHz frequency and 1 W power along the extrusion lines: (a) extrusion lines 1 and 2, and (b) extrusion lines 3 and 4.

distribution must be accounted for in EM safety evaluations, particularly for individuals with cranial implants exposed to 5G radiation.

5. Discussion

5.1. *Key findings*

The findings of this study have potential implications across multiple sectors. In healthcare, the results may assist clinicians and biomedical engineers in assessing the safety of patients with metallic cranial implants exposed to electromagnetic radiation. In telecommunications, the analysis may contribute to the design of wireless devices and antennas that minimize localized electromagnetic exposure. From a public protection perspective, the results may support regulatory bodies in evaluating exposure safety for individuals with implants.

In the present study, the results obtained from the 2D head model show good agreement with previously reported 2D studies in the literature [15,29,30]. Although the use of a 2D model involves geometric simplifications, the qualitative trends and relative distributions of SAR and temperature are also generally consistent with those reported in 3D head models [27,31–33]. This consistency supports the physical reliability of the model and justifies its use as a computationally efficient approach for exposure analysis. Furthermore, the influence of EM absorption in the presence of implants should be carefully considered in safety evaluations, particularly for individuals with cranial implants exposed to 5G radiation.

5.2. *Mechanistic insights*

The study highlights localized electric field enhancement in the presence of metallic implants, which can lead to increased SAR and temperature rise in surrounding tissues. These effects arise from the interaction between EM waves and conductive implant materials, resulting in localized field concentration. The magnitude of these effects depends on factors such as implant geometry, material properties, and frequency, emphasizing the importance of considering implant characteristics in EM exposure assessments.

5.3. *Limitations*

The present study has several limitations. First, it is based solely on deterministic numerical simulations without experimental validation due to limitations in resources and facilities. Second, the use of a 2D axisymmetric head model introduces geometric simplifications and cannot fully capture complex three-dimensional EM interactions, which may affect the accuracy of hotspot localization. Third, an insulated (adiabatic) boundary condition is applied at the outer surface, neglecting heat dissipation to the surrounding environment and potentially overestimating temperature rise. Fourth, tissue dielectric and thermal properties are assumed constant, whereas they may vary with physiological conditions, influencing SAR and temperature predictions. Finally, the reported SAR values are local (point-based) rather than spatially averaged (e.g., 1 g or 10 g) as defined by the ICNIRP guidelines; therefore, comparisons with safety limits should be interpreted with caution.

5.4. *Practical implications*

The results of this study provide useful insights for implant safety assessment, wireless system design, and regulatory evaluation of EM exposure. The findings highlight the importance of considering implant-induced field enhancement in safety evaluations, which may inform the development of improved exposure guidelines and device designs.

5.5. Future work

Future work will focus on extending the analysis to a broader range of 5G frequencies, longer exposure durations, and different implant materials and geometries to enhance electromagnetic safety assessments. Additionally, a multilayer human head phantom with embedded implants will be developed to replicate realistic tissue dielectric and thermal properties. Controlled experimental studies will be conducted using appropriate antenna systems, and SAR and temperature measurements will be compared with simulation results to assess model accuracy.

Further investigations may explore variations in EM absorption across diverse populations, considering differences in anatomical and tissue properties. Moreover, studies on potential non-thermal effects of EM radiation, including in vitro cell experiments and epidemiological analyses, may provide deeper insights into biological responses and long-term exposure effects in individuals with implanted medical devices.

6. Conclusion

This study investigated the effects of metallic implants on EM wave absorption in a 2D heterogeneous human head model exposed to 5G frequencies (2.6, 3.6, 4.4, and 6 GHz). The impact of implant geometry was analysed by embedding stainless steel 410 implants in two shapes, pin and sphere, within the bone layer. Among all the considered frequencies, 3.6 GHz resulted in the highest EM absorption in the head tissues. The findings reveal that the presence of metallic implants significantly increases the electric field intensity, SAR, and temperature compared to the no-implant case. Maximum electric field (78.78 V/m), SAR (6.42 W/kg), and temperature (37.138 °C) were observed at 3.6 GHz for the pin implant. The skin layer consistently exhibited the highest EM absorption due to its proximity to the radiation source and relatively high dielectric properties. Additionally, EM energy absorption across different tissues varied based on their dielectric and thermal characteristics. The SAR values exceeded the ICNIRP safety limit of 2 W/kg in all scenarios except at 6 GHz without an implant. Although, the observed temperature rise remained within the general thermal safety threshold, the presence of metallic implants led to localized heating and shifted hotspot regions, indicating a redistribution of thermal energy. The coupled multiphysics 2D heterogeneous head model provides significant computational time savings for different 5G frequencies and implant geometries, while maintaining good agreement with the literature.

CRediT authorship contribution statement

Deepshikha Bhargava: Writing – review & editing, Writing – original draft, Visualization, Validation, Project administration, Methodology, Investigation, Funding acquisition, Formal analysis, Data curation, Conceptualization. **Phadungsak Rattanadecho:** Supervision, Software, Resources.

Declaration of competing interest

The authors declare that they have no known competing financial interests or personal relationships that could have appeared to influence the work reported in this paper.

Acknowledgments

This project is funded by National Research Council of Thailand (NRCT) (Grant No. N42A680088).

Data availability

Data will be made available on request.

References

[1] T.S. Rappaport, et al., Millimeter wave mobile communications for 5G cellular: It Will Work!, IEEE Access 1 (2013) 335–349, https://doi.org/10.1109/ACCESS.2013.2260813.
[2] A.E.C. Redondi, C. Innamorati, S. Gallucci, S. Fiocchi, F. Matera, A survey on future millimeter-wave communication applications, IEEE Access 12 (2024) 133165–133182, https://doi.org/10.1109/ACCESS.2024.3438625.
[3] M. Simkó and M. O. Mattsson, "5G Wireless Communication and Health Effects-A Pragmatic Review Based on Available Studies Regarding 6 to 100 GHz," (in eng), *Int J Environ Res Public Health,* vol. 16, no. 18, Sep 13 2019, doi: 10.3390/ijerph16183406.
[4] A. Di Ciaula, Towards 5G communication systems: Are there health implications? (in eng), Int J Hyg Environ Health 221 (3) (2018) 367–375, https://doi.org/10.1016/j.ijheh.2018.01.011.
[5] A.B. Miller, L.L. Morgan, I. Udasin, D.L. Davis, Cancer epidemiology update, following the 2011 IARC evaluation of radiofrequency electromagnetic fields (Monograph 102), (in eng), Environ Res 167 (2018) 673–683, https://doi.org/10.1016/j.envres.2018.06.043.
[6] L. Chiaraviglio, et al., Planning 5G networks under EMF constraints: state of the art and vision, IEEE Access 6 (2018) 51021–51037, https://doi.org/10.1109/ACCESS.2018.2868347.
[7] F. de Vocht, P. Albers, The population health effects from 5G: controlling the narrative (in eng), Front Public Health 10 (2022) 1082031, https://doi.org/10.3389/fpubh.2022.1082031.
[8] "Guidelines for Limiting Exposure to Electromagnetic Fields (100 kHz to 300 GHz)," (in eng), *Health Phys,* vol. 118, no. 5, pp. 483-524, May 2020, doi: 10.1097/hp.0000000000001210.
[9] W. H. Bailey *et al.*, "Synopsis of IEEE Std C95.1™-2019 "IEEE Standard for Safety Levels With Respect to Human Exposure to Electric, Magnetic, and Electromagnetic Fields, 0 Hz to 300 GHz"," *IEEE Access,* vol. 7, pp. 171346-171356, 2019, doi: 10.1109/ACCESS.2019.2954823.
[10] T. Wessapan, S. Srisawatdhisukul, and P. Rattanadecho, "Numerical Analysis of Specific Absorption Rate and Heat Transfer in the Human Body Exposed to Leakage Electromagnetic Field at 915 MHz and 2450 MHz," *J. Heat. Transf.,* vol. 133, no. 5, 2011, doi: 10.1115/1.4003115.
[11] D. Bhargava, N. Leeprechanon, P. Rattanadecho, T. Wessapan, Specific absorption rate and temperature elevation in the human head due to overexposure to mobile phone radiation with different usage patterns, Int. J. Heat Mass Transf. 130 (2019) 1178–1188, https://doi.org/10.1016/j.ijheatmasstransfer.2018.11.031.
[12] D. Bhargava, P. Rattanadecho, Numerical analysis of specific absorption rate and temperature distribution in human eye due to moving electromagnetic source, Eng. Sci. 21 (2023) 796, https://doi.org/10.30919/es8d796.
[13] B. Deepshikha and R. Phadungsak, "Effect of Different Positions of Waveguide Port on the Coupled Model of Electromagnetic Wave and Heat Transfer in Microwave Heating of Coal," *Science & Technology Asia,* vol. 27, no. 4, pp. 363-373, 12/31 2022. [Online]. Available: https://ph02.tci-thaijo.org/index.php/SciTechAsia/article/view/247931.
[14] B. Awada *et al.*, "Simulation of the Effect of 5G Cell Phone Radiation on Human Brain," *2018 IEEE International Multidisciplinary Conference on Engineering Technology (IMCET),* pp. 1-6, 2018, doi: 10.1109/IMCET.2018.8603063.
[15] Z.M. Lwin, M. Yokota, Numerical analysis of SAR and temperature distribution in two dimensional human head model based on FDTD parameters and the polarization of electromagnetic wave, AEU – Int. J. Electron. Commun. 104 (2019) 91–98, https://doi.org/10.1016/j.aeue.2019.03.010.
[16] F. Kaburcuk, A.Z. Elsherbeni, Efficient computation of SAR and temperature rise distributions in a human head at wide range of frequencies due to 5 G RF field exposure, Appl. Comput. Electromagn. Soc. J. 33 (11) (2021) 1236–1242.
[17] W.G. Whittow, C.J. Panagamuwa, R.M. Edwards, J.C. Vardaxoglou, The energy absorbed in the human head due to ring-type jewelry and face-illuminating mobile phones using a dipole and a realistic source, IEEE Trans. Antennas Propag. 56 (12) (2008) 3812–3817, https://doi.org/10.1109/TAP.2008.2007353.
[18] W.G. Whittow, R.M. Edwards, A study of changes to specific absorption rates in the human eye close to perfectly conducting spectacles within the radio frequency range 1.5 to 3.0 GHz, IEEE Trans. Antennas Propag. 52 (12) (2004) 3207–3212, https://doi.org/10.1109/TAP.2004.836417.
[19] D. Bhargava, P. Rattanadecho, T. Wessapan, The effect of metal objects on the SAR and temperature increase in the human head exposed to dipole antenna (numerical analysis), Case Stud. Therm. Eng. 22 (2020) 100789, https://doi.org/10.1016/j.csite.2020.100789.
[20] T. Wessapan, P. Rattanadecho, Thermal effects of metal implants embedded in different layers of human tissues exposed to electromagnetic fields, Case Stud Therm. Eng. 53 (2024) 103771, https://doi.org/10.1016/j.csite.2023.103771.
[21] H. Virtanen, J. Keshvari, R. Lappalainen, The effect of authentic metallic implants on the SAR distribution of the head exposed to 900, 1800 and 2450 MHz dipole near field, Phys. Med. Biol. 52 (5) (2007) 1221–1236, https://doi.org/10.1088/0031-9155/52/5/001.
[22] C. J. Panagamuwa, W. G. Whittow, R. M. Edwards, and J. C. Vardaxoglou, "A Study of the Effects of Metallic Pins on SAR using a Specific Anthropomorphic Mannequin (SAM) Head Phantom," in *The Second European Conference on Antennas and*

Propagation, EuCAP 2007, 11-16 Nov. 2007 2007, pp. 1-6, doi: 10.1049/ic.2007.0987.
[23] B. Hocking, K.H. Joyner, A.H. Fleming, Implanted medical devices in workers exposed to radio-frequency radiation (in eng), Scand J Work Environ Health 17 (1) (1991) 1–6, https://doi.org/10.5271/sjweh.1740.
[24] C. Gabriel, "Compilation of the Dielectric Properties of Body Tissues at RF and Microwave Frequencies," 1996.
[25] D. Chen and B. Zhang, "Electromagnetic Exposure Assessment of 5G Mobile Phones: SAR and Thermal Distribution in a Multi-Layer Human Head Model," *Sensors,* vol. 26, no. 5, p. 1468, 2026. [Online]. Available: https://www.mdpi.com/1424-8220/26/5/1468.
[26] J. Li, Q. Zhang, and M. Lu, "Electromagnetic Exposure from RF Antennas on Subway Station Attendant: A Thermal Analysis," *Sensors,* vol. 26, no. 2, p. 709, 2026. [Online]. Available: https://www.mdpi.com/1424-8220/26/2/709.
[27] T. Wessapan and P. Rattanadecho, "Numerical Analysis of Specific Absorption Rate and Heat Transfer in Human Head Subjected to Mobile Phone Radiation: Effects of User Age and Radiated Power," *J. Heat. Transf.,* vol. 134, no. 12, 2012, doi: 10.1115/1.4006595.
[28] H.H. Pennes, Analysis of tissue and arterial blood temperatures in the resting human forearm, J. Appl. Physiol. 1 (2) (1948) 93–122, https://doi.org/10.1152/jappl.1948.1.2.93.
[29] A. I. Sabbah and N. I. Dib, "Evaluation of SAR and Temperature Elevation in a Multi-layered Human Head Model Exposed to RF Radiation," 2010.
[30] A.A. Omar, Q.M. Bashayreh, A.M. Al-Shamali, Investigation of the effect of obliquely incident plane wave on a human head at 900 and 1800 MHz, Int. J. RF Microwave Comput. Aided Eng. 20 (2) (2010) 133–140, https://doi.org/10.1002/mmce.20402.
[31] T. Wessapan, S. Srisawatdhisukul, P. Rattanadecho, Specific absorption rate and temperature distributions in human head subjected to mobile phone radiation at different frequencies, Int. J. Heat Mass Transf. 55 (1) (2012) 347–359, https://doi.org/10.1016/j.ijheatmasstransfer.2011.09.027.
[32] V. Stanković, D. Jovanović, D. Krstić, V. Marković, N. Cvetković, Temperature distribution and specific absorption rate inside a child's head, Int. J. Heat Mass Transf. 104 (2017) 559–565, https://doi.org/10.1016/j.ijheatmasstransfer.2016.08.094.
[33] A. Hadjem, D. Lautru, C. Dale, W. Man Fai, V.F. Hanna, J. Wiart, Study of specific absorption rate (SAR) induced in two child head models and in adult heads using mobile phones, IEEE Trans. Microw. Theory Tech. 53 (1) (2005) 4–11, https://doi.org/10.1109/TMTT.2004.839343.